Mon. Not. R. Astron. Soc. **000**, 000–000 (0000) Printed 17 June 2015 (MN LATEX style file v2.2)

Lyman-α emitters gone missing: evidence for late reionization?

Tirthankar Roy Choudhury[1], Ewald Puchwein[2], Martin G. Haehnelt[2] and James S. Bolton[3]

[1] *National Centre for Radio Astrophysics, Tata Institute of Fundamental Research, Pune 411007, India*
[2] *Institute of Astronomy and Kavli Institute for Cosmology, University of Cambridge, Madingley Road, Cambridge CB3 0HA, UK*
[3] *School of Physics and Astronomy, University of Nottingham, University Park, Nottingham, NG7 2RD, UK*

arXiv:1412.4790v2 [astro-ph.CO] 16 Jun 2015

17 June 2015

ABSTRACT

We combine high resolution hydrodynamical simulations with an intermediate resolution, dark matter only simulation and an analytical model for the growth of ionized regions to estimate the large scale distribution and redshift evolution of the visibility of Lyα emission in $6 \leq z \leq 8$ galaxies. The inhomogeneous distribution of neutral hydrogen during the reionization process results in significant fluctuations in the Lyα transmissivity on large scales. The transmissivity depends not only on the ionized fraction of the intergalactic medium by volume and the amplitude of the local ionizing background, but is also rather sensitive to the evolution of the relative velocity shift of the Lyα emission line due to resonant scattering. We reproduce a decline in the space density of Lyα emitting galaxies as rapid as observed with a rather rapidly evolving neutral fraction between $z = 6 - 8$, and a typical Lyα line velocity offset of $100\,\mathrm{km\,s^{-1}}$ redward of systemic at $z = 6$ which decreases toward higher redshift. The new (02/2015) Planck results indicate such a recent end to reionization is no longer disfavoured by constraints from the cosmic microwave background.

Key words: dark ages, reionization, first stars – intergalactic medium – cosmology: theory – large-scale structure of Universe.

1 INTRODUCTION

Colour selection techniques applied to deep imaging surveys with Advanced Camera for Surveys on the Hubble Space Telescope have enabled the routine identification of large numbers of high redshift galaxies out to redshifts as high as $z = 10$, deep in the epoch of hydrogen reionization (for recent results, see Labbé et al. 2013; Oesch et al. 2013; Bouwens et al. 2013, 2015; Oesch et al. 2014; Finkelstein et al. 2014; McLeod et al. 2014). The evolution of the galaxy luminosity function inferred from these surveys thereby appears smooth with a rather modest decrease of the space density of continuum emission selected galaxies with increasing redshift.

This rather smooth evolution of continuum selected galaxies is, however, not mirrored by the Lyα emission from high redshift galaxies, which appears to decline rather rapidly at $z > 6$. This was first noted in Lyα emission selected galaxy samples (Kashikawa et al. 2006) and has been since confirmed by several Lyα emitter surveys (Ouchi et al. 2010; Hu et al. 2010; Kashikawa et al. 2011; Konno et al. 2014). It has also been established for continuum selected galaxies by a careful investigation of their Lyα equivalent width distribution (Fontana et al. 2010; Stark et al. 2011; Pentericci et al. 2011; Schenker et al. 2012; Treu et al. 2012; Caruana et al. 2012; Pentericci et al. 2014; Caruana et al. 2014; Schenker et al. 2014; Tilvi et al. 2014). This rapid evolution of the Lyα emission in high redshift galaxies was initially surprising; reionization models had predicted that the intergalactic medium (IGM) needed to still be substantially neutral (with volume averaged neutral fractions > 50 per cent at $z \sim 7$) for not yet reionized gas to strongly affect the visibility of Lyα emission from high-redshift galaxies (Pentericci et al. 2011; Ono et al. 2012; Schenker et al. 2012; Jensen et al. 2013; Konno et al. 2014; Faisst et al. 2014).

There is, however, now a general consensus that the Universe is mostly ionized at $z \sim 6$, based on detailed analyses of QSO absorption spectra (Fan et al. 2006; Gallerani et al. 2006, 2008; Raskutti et al. 2012; McGreer et al. 2015). Both CMB data and the ionizing emissivity inferred from QSO absorption spectra and high-redshift galaxy surveys also suggest that large neutral hydrogen fractions of fifty per cent or more are only expected to be present at redshift $z > 7$ (Pritchard et al. 2010; Mitra et al. 2011; Kuhlen &

© 0000 RAS

Faucher-Giguère 2012; Mitra et al. 2012; Robertson et al. 2013). It has therefore been argued that the rapid evolution of the Lyα emission in high-redshift galaxies may be due to a rapid evolution of the internal properties of high redshift galaxies with regard to the escape of Lyα emission (Dayal & Ferrara 2012). While this could certainly explain the rapid demise of Lyα emission, there are, however, concerns about the plausibility of such a rapid evolution within the smoothly evolving hierarchical paradigm for galaxy formation suggested by the ΛCDM cosmological framework. Alternatively, Dijkstra et al. (2014) have argued that an evolving Lyman continuum escape fraction may in part explain the observed Lyα emitter (LAE) evolution, while Taylor & Lidz (2014) note that sample variance could also play a role due to the patchy nature of reionization.

Motivated by these findings, along with the possible discovery of a damping wing that extends redwards of the systemic host galaxy redshift in an (absorption) spectrum of the $z = 7.085$ QSO ULAS J1120+0641 (Mortlock et al. 2011; Bolton et al. 2011), Bolton & Haehnelt (2013) performed detailed numerical modelling of the Lyα opacity during the epoch of reionization. Their simulations employed sufficient resolution to account for the opacity due to self-shielded residual neutral hydrogen in the already mostly ionized regions of the Universe. In this way, Bolton & Haehnelt (2013) demonstrated that self-shielded neutral regions in the late stages of reionization can lead to substantial Lyα opacity even for volume filling factors of neutral hydrogen as low as ten percent, potentially explaining the observed rapid decline of LAEs. However, the simulations of Bolton & Haehnelt (2013) were performed with a volume too small to investigate the spatial distribution and evolution of the intervening Lyα opacity. They were furthermore based on a simple backwards extrapolation of photoionization rates measured at lower redshift, and lacked a realistic model for the growth of ionized regions. The most recent Planck results (Planck Collaboration et al. 2015) also now appear to be fully consistent with models predicting reionization to complete not much before $z \sim 6$, somewhat relaxing the need for low (~ 10 per cent) neutral hydrogen fractions at $z \sim 7$.

To investigate this further we therefore combine high-resolution hydrodynamical simulations which reproduce the observed IGM Lyα opacity at $2 < z < 6$ with an analytical model for the growth of ionized regions built on a large, dark matter only simulation. Our analytical model for the growth of ionized regions is based on that described in Zahn et al. (2007), Choudhury et al. (2009) and Majumdar et al. (2012), and has been successfully tested against cosmological radiative transfer simulations (Mellema et al. 2006; Iliev et al. 2012) in Majumdar et al. (2014). The hybrid approach we employ here is thus similar to that presented in Mesinger et al. (2015), but note that we calibrate our model for the growth of ionized regions to match observations of photoionization rate (Wyithe & Bolton 2011; Calverley et al. 2011) and mean free path of ionizing photons (Songaila & Cowie 2010; Worseck et al. 2014) at $5 \lesssim z \lesssim 6$. Our default model for the evolution of the volume filling factor of ionized regions is thereby chosen to be close to that predicted by the recent update of the Haardt & Madau (2012) metagalactic UV background model (HM2012 hereafter), which incorporates a wide range of recent observational constraints. However, we shall also explore the effect of reionization completing somewhat later than in the HM2012 model. We use our hybrid technique not only to make predictions for the probability distribution of Lyα transmissivity due to the increasingly neutral, inhomogeneously reionized intervening IGM, but we also investigate the large-scale spatial distribution of the transmissivity.

The paper is structured as follows. In Section 2 we describe our numerical simulations, and in Section 3 we discuss the spatial distribution of neutral hydrogen and the reionization history within our hybrid simulations. Section 4 outlines our results, including predictions for the spatial distribution of the Lyα emission line transmissivity under a wide variety of model assumptions. We conclude in Section 5. A flat ΛCDM cosmological model with $\Omega_m = 0.305$, $\Omega_b = 0.048$, $h = 0.679$, $n_s = 0.96$, $\sigma_8 = 0.827$ is adopted throughout (Planck Collaboration et al. 2014).

2 THE SPATIAL DISTRIBUTION OF NEUTRAL HYDROGEN

2.1 The need for a hybrid technique

Simulating the spatial distribution of neutral hydrogen during and after reionization is a computationally very demanding task. The typical sizes of ionized regions before overlap are several tens of (comoving) Mpc, while the scale of the optically thick regions acting as sinks of ionizing photons in already ionized regions are only tens of kpc. Simulations that follow the growth of ionized regions therefore require box sizes of hundred cMpc or more, while modelling the Lyα opacity correctly requires high-resolution hydrodynamical simulations for which achievable box sizes are typically ten h^{-1} cMpc.

In order to achieve this dynamic range, we therefore employ a hybrid technique where we calculate the growth of ionized regions with a well tested analytical method which relates the growth of structure as probed by collapsed dark matter haloes to the production of ionizing photons (Zahn et al. 2007; Choudhury et al. 2009; Majumdar et al. 2012, 2014). We apply this technique to a 1200^3 particle, large ($100\,h^{-1}$ cMpc) collisionless dark matter simulation with moderate resolution. The hydrogen distribution in the ionized regions is then modelled by replicating a smaller 2×512^3 particle, $10\,h^{-1}$ cMpc high-resolution hydrodynamical simulation on top of the ionization structure from the larger box. In the following, we will refer to these two models simply as the "large box" and "small box" simulations, respectively.

A 2×5120^3 particle hydrodynamical simulation would have been required to achieve the same mass resolution within a $100\,h^{-1}$ cMpc box, which is still beyond even the most ambitious current state-of-the-art hydrodynamical simulations of the IGM (Vogelsberger et al. 2014; Lukić et al. 2015; Schaye et al. 2015). Note, however, that the hybrid simulation neither captures the large scale power in the density field nor the correlation between the morphology of the large scale ionized regions and the local density field. On average, the density of gas and the abundance of collapsed structures will thus be underestimated in ionized bubbles; they correspond to dense regions in the large box, but are populated with small boxes of mean density in the

hybrid simulation. Our models may therefore underestimate the number of absorbers in ionized bubbles. On the other hand, our hybrid simulation assumes a constant background photoionization rate within the ionized regions, which may lead to overestimation of the number of absorbers close to sources where the actual photoionization rate is expected to be higher than average.

2.2 Modelling the growth of ionized regions

To model the growth of ionized regions we need a model for the production of ionizing photons. Simple models that relate the integrated number of ionizing photons in a given region to either dark matter haloes or the collapsed mass fraction smoothed on a suitable scale have been shown to reproduce the results of much more demanding, full radiative transfer simulations (Mellema et al. 2006; Iliev et al. 2012) remarkably well (Majumdar et al. 2014). We employ here the model based on Zahn et al. (2007) and Choudhury et al. (2009) and apply it to our large box simulation, which is dark-matter only, run using the P-GADGET3 N-body code (the previous version of the code is publicly available[1] and is described in Springel 2005).

We first briefly describe the basic steps of this model, which is similar to that in Zahn et al. (2007) and identical to the method described in Choudhury et al. (2009) (the $\epsilon = 0$ case in their paper) and Majumdar et al. (2014) (the "semnum" model). As a first step we use a FoF halo finder to identify the locations and masses of the dark matter haloes in the large box. We require a group to have at least 32 particles to be labelled as a halo, thus giving a minimum halo mass of $1.57\times10^9 h^{-1}$ M$_\odot$. This minimum mass is larger than the typical mass of atomically cooled haloes with $T_{\rm vir} \sim 10^4$ K, but is similar to the threshold mass in regions which are affected by radiative feedback from reionization. Since we are interested in the late stages of the reionization history where most of the IGM is heated, the lack of smaller mass haloes in the simulation box should not impact significantly on our results.

The haloes are assigned emissivities proportional to the halo mass and are subsequently used for generating the ionization field. A given location $\mathbf{x}$ in the simulation box is assumed to be ionized if, within a spherical region of radius R around it, the condition

$$\zeta_{\rm eff} f_{\rm coll}(\mathbf{x}, R) \geq 1, \qquad (1)$$

is satisfied for any value of R, where $f_{\rm coll}(\mathbf{x}, R)$ is the collapsed mass fraction within the spherical volume[2]. The parameter $\zeta_{\rm eff}$ is the effective ionizing efficiency, which corresponds to the number of photons in the IGM per hydrogen in stars, compensated for the number of hydrogen recombinations in the IGM. The large-scale ionization field at a given redshift is thus determined by only one parameter, $\zeta_{\rm eff}$. Note that we do not yet model the regions optically thick to ionizing radiation ("Lyman-limit systems") while generating the ionization maps from the large box. We will take care of these separately using the small box to model the small scale neutral hydrogen distribution assuming an ionization rate consistent with that used in the large box.

In Figure 1 we show maps of the neutral hydrogen fraction at $z = 8$, 7 and 6 at the tail-end of hydrogen reionization for two models of the evolution of the ionized mass fraction that we have calibrated to match current observational constraints on the photoionization rates at $z \leq 6$. The calibration procedure is described in detail in Sec. 3. In the next section, we proceed to describe our modelling of the optically thick regions within ionized bubbles using the small box.

2.3 Modelling the optically thick systems acting as sinks of ionizing photons

The large box simulation is appropriate for studying large-scale fluctuations in the ionizing emissivity. However, it does not resolve the very small scales which are required to model the optically thick absorption systems (i.e., the (super) Lyman-limit systems). Modelling such systems requires simulations with spatial resolution as small as ~ 10 ckpc. We have thus used a smoothed particle hydrodynamics simulation using P-GADGET3 with a box size of $10\,h^{-1}$ cMpc and 2×512^3 dark matter and gas particles, similar to the model used in Bolton & Haehnelt (2013).

We model the distribution of optically thick absorption systems in the small box as follows. Given the value for the background photoionization rate in the IGM, $\Gamma_{\rm HI}$, one can obtain the neutral hydrogen fraction at any location assuming photoionization equilibrium. However, although this approach is reasonably accurate in modelling the low density optically thin IGM, it is not appropriate for self-shielded regions. To account for this in the past it has often been assumed that the gas remains neutral above a density threshold $\Delta_{\rm ss}$. Assuming the size of the system to be given by the Jeans scale (Schaye 2001), the threshold density is then,

$$\Delta_{\rm ss} = 36 \left(\frac{\Gamma_{\rm HI}}{10^{-12}{\rm s}^{-1}}\right)^{2/3} \left(\frac{T}{10^4{\rm K}}\right)^{2/15} \times \left(\frac{\mu}{0.61}\right)^{1/3} \left(\frac{f_e}{1.08}\right)^{-2/3} \left(\frac{1+z}{8}\right)^{-3}, \qquad (2)$$

where T is the gas temperature, μ is the mean molecular weight and $f_e = n_e/n_H$ is the ratio of free electrons to hydrogen. The threshold can be computed at every location in the simulation box using the densities and temperatures of the gas particles. According to equation (2), low values of $\Gamma_{\rm HI}$ at high redshift can make $\Delta_{\rm ss}$ unrealistically small. In the models we use in this paper, this starts to affect our analysis at $z > 8$. To avoid this, we impose a lower limit of $\Delta_{\rm ss} \geq 2$ on the self-shielding threshold.

In this work we consider three different models; one that neglects self-shielding, one with a simple density threshold for self-shielding (i.e. Eq. 2) and one where self-shielding is implemented with a fitting formula based on full radiative transfer simulations. These are summarized as follows:

- **No-SS:** self-shielding is neglected in this model. The IGM is assumed to be optically thin and in photoionization equilibrium at every location within the ionized regions found in the large box, irrespective of the local density.

[1] `http://www.mpa-garching.mpg.de/gadget/`

[2] Points which do not satisfy condition (1) are assigned an ionized fraction $\zeta_{\rm eff} f_{\rm coll}(\mathbf{x}, R_{\rm min})$, where $R_{\rm min}$ is the spatial resolution of the grid which is used for generating the ionization field.

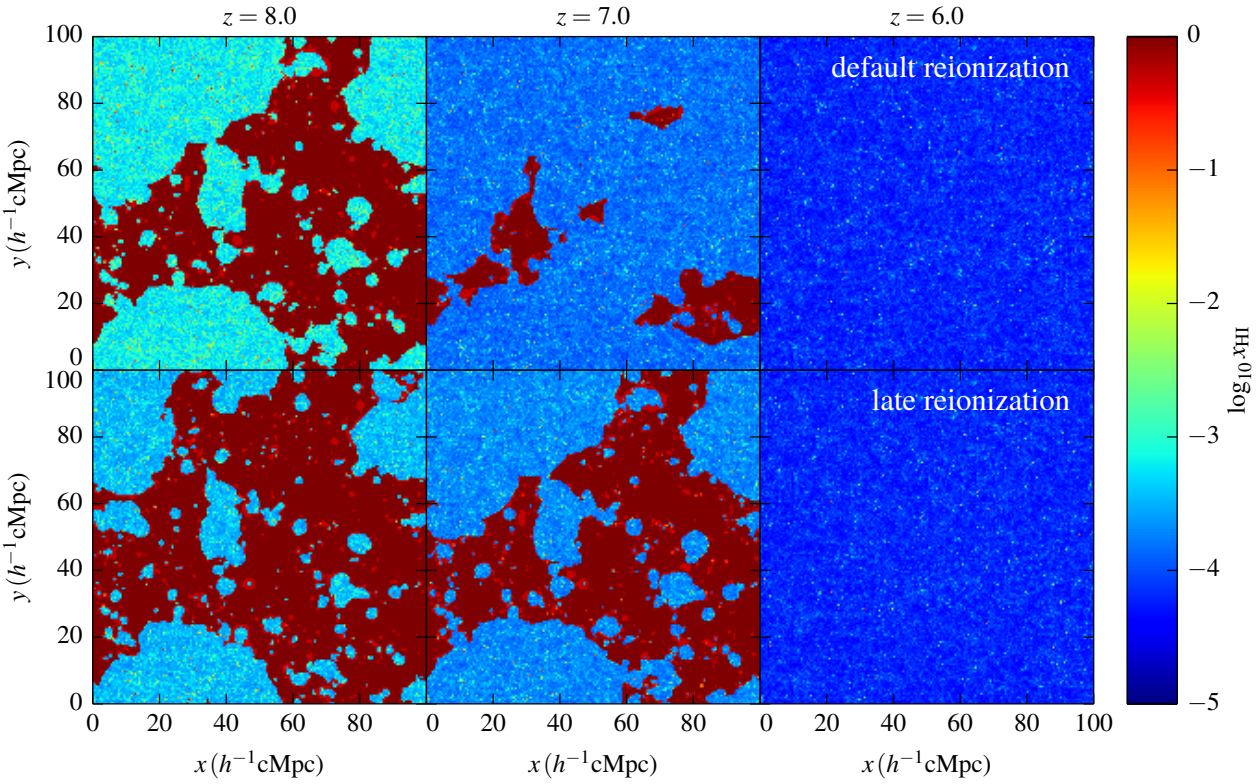

Figure 1. Maps of the neutral hydrogen fraction at $z = 8, 7$ and 6, obtained with our analytic method for modelling the growth of ionized regions within our large simulation box. The *top* panels show our default reionization model, while the *bottom* panels show our late reionization model.

• **SS:** Hydrogen is assumed to be completely neutral if $\Delta_H > \Delta_{\rm ss}$, i.e.,

$$\Gamma_{\rm HI}^{\rm local} = \begin{cases} \Gamma_{\rm HI} & \text{when } \Delta_H \leq \Delta_{\rm ss}, \\ 0 & \text{if } \Delta_H > \Delta_{\rm ss}, \end{cases} \tag{3}$$

where Δ_H is the hydrogen overdensity.

• **SS-R:** The SS model predicts a transition in the ionization state around the threshold density which is sharper than found in radiative transfer simulations involving recombinations (Rahmati et al. 2013). In this third model we therefore use the empirical fit provided by Rahmati et al. (2013) to their radiative transfer calculations, where:[3]

$$\frac{\Gamma_{\rm HI}^{\rm local}}{\Gamma_{\rm HI}} = 0.98\left[1+\left(\frac{\Delta_H}{\Delta_{\rm ss}}\right)^{1.64}\right]^{-2.28} + 0.02\left[1+\frac{\Delta_H}{\Delta_{\rm ss}}\right]^{-0.84}. \tag{4}$$

The spatial distribution of the neutral hydrogen fraction, $n_{\rm HI}/n_H$, obtained using these different models are compared in Figure 2. The redshift chosen is $z = 7$ and results are shown for two background photoionization rates $\log_{10}(\Gamma_{\rm HI}/{\rm s}^{-1}) = -12.8$ and -13.6. The occurrence of fully neutral regions is almost negligible for the No-SS case. In the SS model the presence of overdense regions with $x_{\rm HI} = 1$ is quite prominent. In comparison, as discussed by Keating et al. (2014) and Mesinger et al. (2015) the effect of self-shielding in the radiative transfer motivated SS-R model is considerably reduced. The volume-averaged neutral hydrogen fraction, $\bar{x}_{\rm HI}^V$, for the three models is listed in Table 1.

[3] The relation we have used for estimating the self-shielding threshold, Eq. (2), differs slightly from that used in Rahmati et al. (2013), particularly the T-dependence of $\Delta_{\rm ss}$. However, the difference in the predicted photoionization rate is not more than ~ 10 per cent.

Model	$\bar{x}_{\rm HI}^V$	
	$\log_{10}(\Gamma_{\rm HI}/{\rm s}^{-1}) = -13.6$	$\log_{10}(\Gamma_{\rm HI}/{\rm s}^{-1}) = -12.8$
No-SS	2.1×10^{-3}	3.4×10^{-4}
SS	3.0×10^{-2}	2.6×10^{-3}
SS-R	6.5×10^{-3}	6.3×10^{-4}

Table 1. The volume-averaged residual neutral hydrogen fraction at $z = 7$ for the self-shielding models displayed in Fig. 2.

3 CALIBRATING THE REIONIZATION HISTORY IN THE HYBRID SIMULATION

3.1 Constructing the hybrid simulation

We now turn to describe how we combine the small and large boxes in our hybrid approach and calibrate the reionization history. This involves replicating the small box and superimposing the large scale ionization map from the large box. The baryonic density field in the hybrid box is calculated using only the small box, while the peculiar velocity field is obtained by adding the large-scale modes from the large

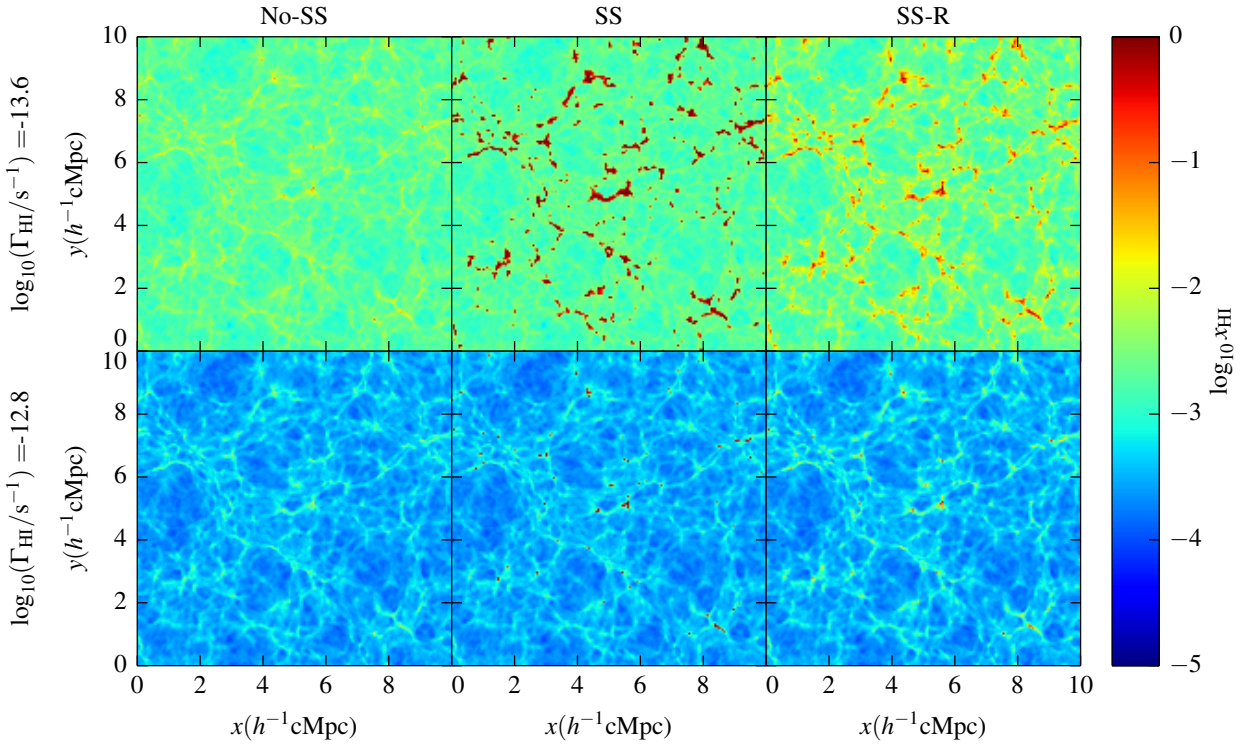

Figure 2. The residual neutral hydrogen fraction in our small box at $z = 7$. For the purpose of this comparison, we have assumed the small box lies entirely within an ionized region in our large box. Results are shown for different values of the background photoionization rate, $\bar{\Gamma}_{\rm HI} = -13.6$ (top) and -12.8 (bottom), and for the three different treatments of self-shielding we consider (from left to right, No-SS, SS and SS-R).

box to the velocity field of the small box (the details of this procedure are discussed in Appendix B). Figure 3 illustrates this approach, where we exploit the periodicity of the simulation and apply a random translation and rotation to the particle positions and velocities in each copy of the small box. However, in order to correctly include the Lyα opacity of the intervening IGM in this hybrid volume, we must calculate a photoionization rate consistent with the overall ionized fraction of hydrogen in the large box.

There are still rather large uncertainties with regard to the background photoionization rate during reionization. At the tail-end of reionization at $5 < z < 6$, observational data are based on the observed mean transmitted flux and the proximity effect in QSO absorption spectra (Wyithe & Bolton 2011; Calverley et al. 2011). These measurements utilise numerical hydrodynamical simulations which are very similar to our small simulation box. At $z > 6$ the best constraints come from the observed UV luminosity functions of high redshift galaxies (see Robertson et al. 2013, for recent results). Unfortunately the latter probe the UV emissivity somewhat redwards of the Lyman-limit and require considerable extrapolation in order to estimate the ionizing emissivity. As the recently updated UV background model presented by HM2012 takes into account these and other observations, we use this model as benchmark to calibrate the reionization history of our simulation at $z > 6$. We now briefly describe this calibration procedure below. Further details are discussed in Appendix A.

Firstly, in order to compute the Lyα optical depth in the hybrid simulation at each redshift, we require the photoionization rate, $\Gamma_{\rm HI}$, within the ionized bubbles. We estimate this self-consistently by the following iterative process. We start with a trial value of $\Gamma_{\rm HI}$, and for a given self-shielding prescription we may then use this to estimate the average mean free path for ionizing photons, $\lambda_{\rm mfp}$, and the clumping factor of the gas, $\mathcal{C}$, within ionized bubbles (see Appendix A for details). The knowledge of $\lambda_{\rm mfp}$ allows us to estimate the *globally* averaged comoving photon emissivity as (e.g. Kuhlen & Faucher-Giguère 2012; Becker & Bolton 2013)

$$\dot{n}_{\rm ion} = \frac{\Gamma_{\rm HI}\ Q_V}{(1+z)^2 \sigma_H \lambda_{\rm mfp}} \left(\frac{\alpha_b + 3}{\alpha_s} \right), \qquad (5)$$

where α_s is the spectral index of the ionizing sources (in this case, the stars) at $\lambda < 912\,$Å and α_b is the spectral index of the ionizing background. The factor Q_V, which is the ionized fraction by volume, converts the photon emissivity in ionized bubbles to the globally averaged value. The quantity $(\alpha_b+3)/\alpha_s$ is estimated from the model of Haardt & Madau (2012) by computing the ratio $\dot{n}_{\rm ion}\lambda_{\rm mfp}/(\Gamma_{\rm HI}\ Q_V)$.

One can then estimate the time derivative of the *mass*-averaged ionization fraction, Q_M, from the equation (e.g. Madau et al. 1999)

$$\frac{{\rm d}Q_M}{{\rm d}t} = \frac{\dot{n}_{\rm ion}}{n_H} - \frac{Q_M}{t_{\rm rec}}. \qquad (6)$$

The recombination time scale $t_{\rm rec}$ is given by

$$t_{\rm rec} = \frac{1}{\mathcal{C}\ \alpha_R\ \chi\ \bar{n}_H\ (1+z)^3}, \qquad (7)$$

where α_R is the recombination rate coefficient for which we assume the same value as HM2012. We assume that helium

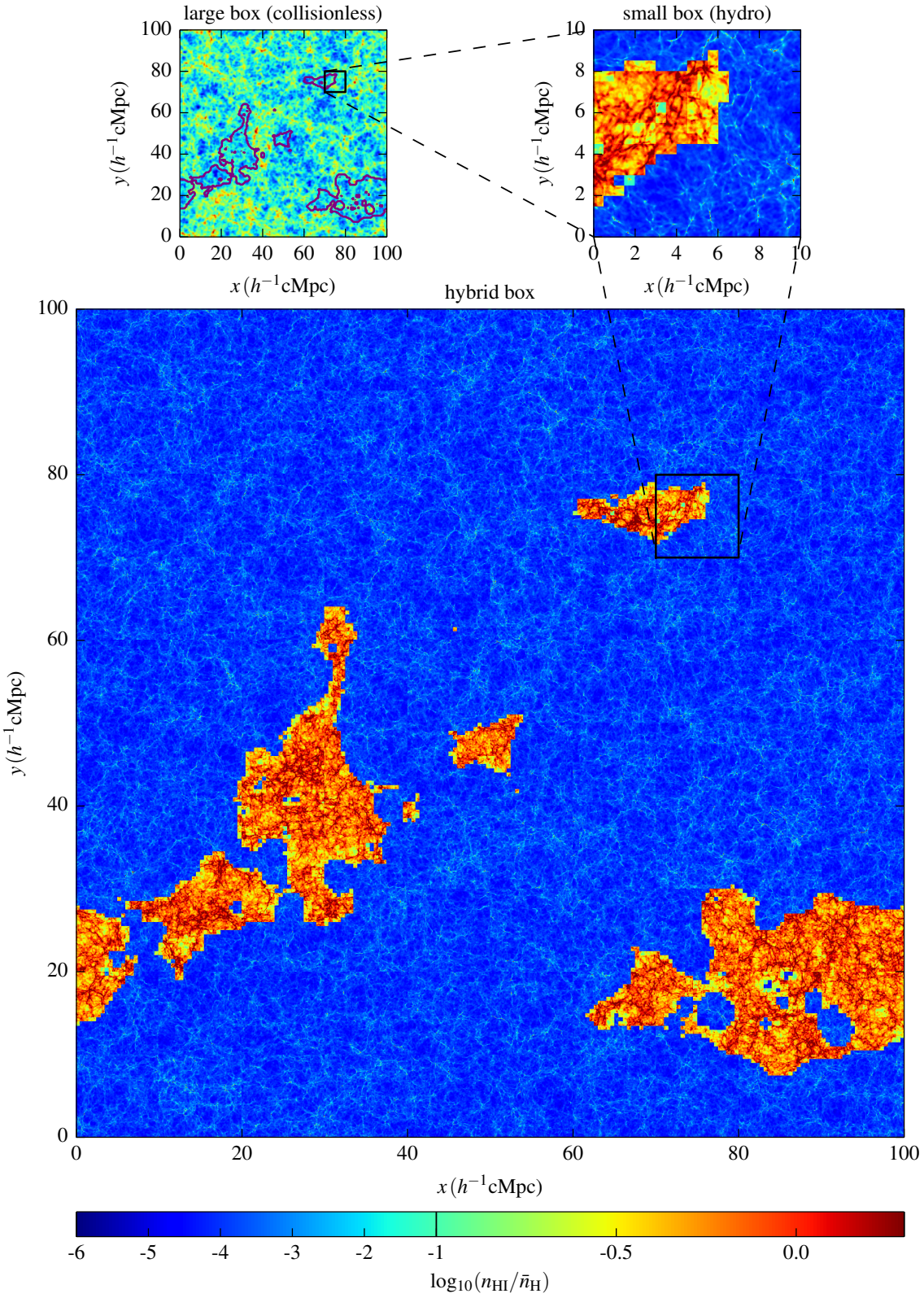

Figure 3. Illustration of the construction of the high-resolution hybrid box including the large scale ionization field at $z = 7$. The *top left* panel shows the large scale density field obtained from the large box of size $100\,h^{-1}$ Mpc, as well as the boundaries of the ionized regions obtained using the analytic model. The *top right* panel displays the neutral hydrogen density in the small box with the map of the ionized regions from the large box applied to it. The *lower* panel shows the neutral hydrogen density in the hybrid box, constructed by populating the volume of the large box with 10^3 randomly shifted and rotated copies of the small box.

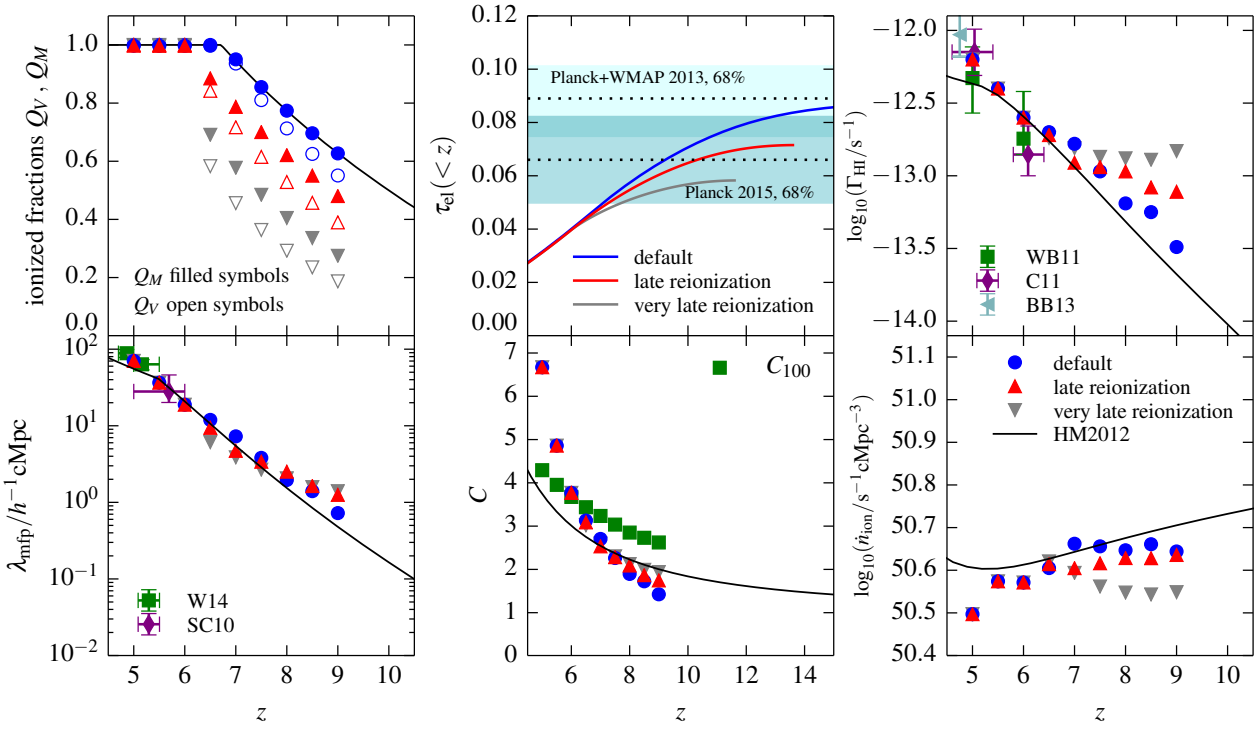

Figure 4. Overview of the main properties of our reionization models. Our default and late reionization models are shown in blue and red, respectively. In light gray is shown a model, called the very late reionization model, where Lyα emitters and ionized regions are assumed to be strongly correlated (see section 4.3 and Appendix C for a detailed discussion). The *black solid* curves show predictions of the HM2012 UV background model for reference. Our models are calibrated by fixing the evolution of the ionized mass fraction, $Q_{\rm M}(z)$. All other quantities are calculated self-consistently. For the default model, $Q_{\rm M}(z)$ was set equal to the ionized fraction in the HM2012 "minimal reionization model". The $Q_{\rm M}(z)$ chosen in our late reionization model is also shown in the *upper left* panel, as well as the ionized volume fractions, $Q_{\rm V}(z)$. The *upper middle* panel compares the optical depth due to Thomson scattering to the Planck 2013 and 2015 results (Planck Collaboration et al. 2014, 2015). The *upper right* panel shows the average hydrogen photoionization rate within ionized regions obtained in our models. Observational constraints from Wyithe & Bolton (2011, WB11), Calverley et al. (2011, C11) and Becker & Bolton (2013, BB13) are shown for reference. The *lower left* panel displays the mean free path of ionizing photons at 1 Ryd measured from our hybrid box. The data is from Worseck et al. (2014, W14) and Songaila & Cowie (2010, SC10). The *lower middle* panel shows the clumping factor in the ionized regions. To allow a direct comparison to the clumping factor used in HM2012, we have also computed the clumping factor $\mathcal{C}_{100}$ of gas below an overdensity of 100. The *lower right* panel shows the globally averaged comoving emission rates of ionizing photons that our models imply, compared to the rate predicted by the HM2012 UV background model.

is singly ionized in H II regions, so that $\chi = 1.08$ is the number of free electrons per hydrogen nucleus.

We then repeat this procedure iteratively until the evolution of Q_M is matched to that of HM2012 at $z < 9$. Thus, for each redshift, we choose a value of ionizing efficiency $\zeta_{\rm eff}$ (see Eq. 1) and $\Gamma_{\rm HI}$ that reproduce the assumed Q_M and ${\rm d}Q_M/{\rm d}t$ at that redshift. Note that this procedure breaks down in the post-reionization era when $Q_M = 1$ and ${\rm d}Q_M/{\rm d}t = 0$. In that case, we assume a value of $\Gamma_{\rm HI}$ which is consistent with observations at $z \sim 5-6$. The Lyα optical depth can be easily computed once $\Gamma_{\rm HI}$ is fixed.

3.2 Reionization histories

The iterative calibration of our model described above allows us to fix one quantity, $Q_M(z)$. All other quantities are then obtained self-consistently from the hybrid simulation box. In this work we will consider three reionization histories:

- **default reionization model:** $Q_M(z)$ is set equal to the ionized fraction in the HM2012 "minimal reionization model", as discussed above.

- **late reionization model:** this model is motivated by the rather rapid evolution in ionized fraction between $z = 6$–8 required to match the Lyα emitter data. We simply shift the $Q_M(z)$ such that the reionization is completed at $z = 6$ (as opposed to 6.7 in HM2012) keeping the value of ${\rm d}Q_M/{\rm d}z$ unchanged.

- **very late reionization model:** this model is introduced in order to match the Lyα emitter data assuming Lyα emitters and ionized regions are strongly correlated (see section 4.3 and Appendix C for a detailed discussion). The ionized fraction in this case evolves more rapidly compared to the other two models.

The mass-averaged ionization fraction, $Q_M(z)$ for the three models is shown in the upper left panel of Figure 4. The figure also displays the evolution of several other quantities describing the progress of reionization, along with a comparison to observations and the HM2012 predictions. By construction, we find good agreement with the observed photoionization rates at $z = 5 - 6$. We also find reasonable

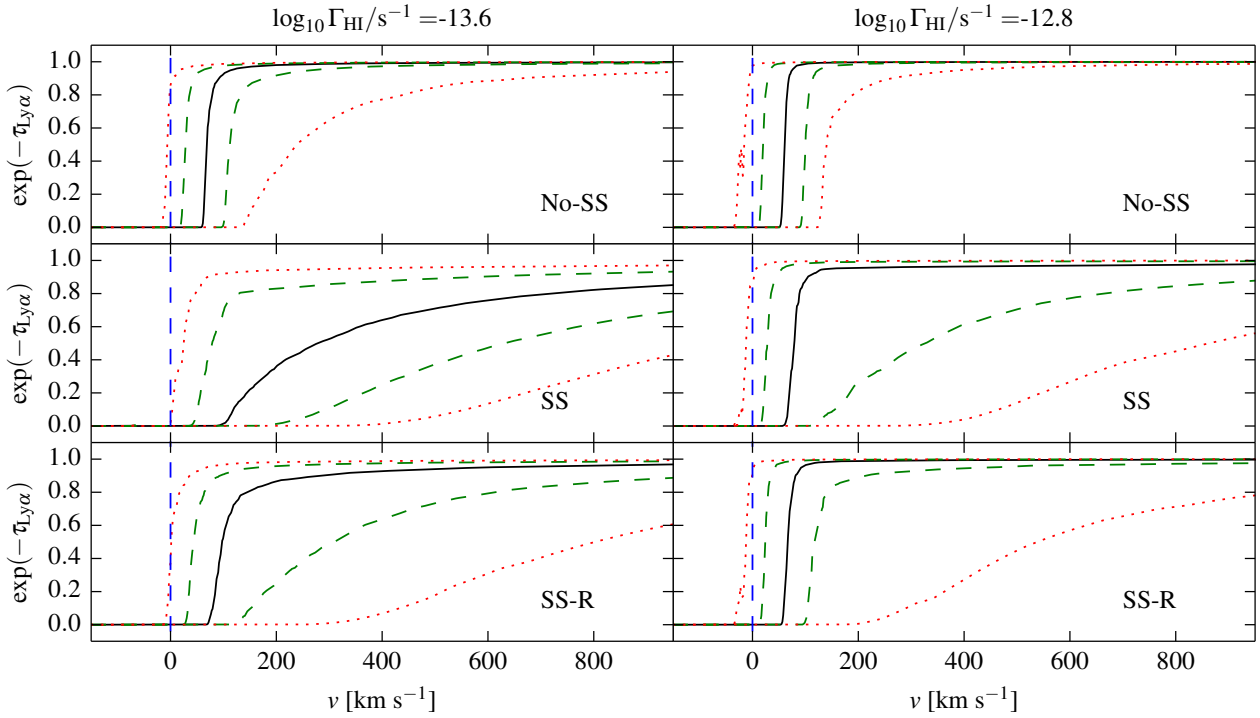

Figure 5. The median and scatter of the Lyα transmission, $e^{-\tau_{\rm Ly\alpha}}$, along individual sightlines obtained from the small box at $z = 7$. The results are shown for three different prescriptions for self-shielding and for two values of the background photoionization rate (assumed to be uniform). The dashed (green) and dotted (red) curves bound 68 and 95 per cent of the Lyα transmission around the median (black curves).

agreement with the observed mean free path at these redshifts. This is not surprising as these have been inferred from the observational data using simulations very similar to our small box. The ionizing emissivity in our default reionization model differs very little ($\lesssim 25\%$) from that assumed in HM2012. The difference is mainly due to a different clumping factor; HM2012 have assumed a fixed density threshold of $\Delta_{\rm ss} = 100$ for self-shielding, while we have calculated it self-consistently. The clumping factor in our models therefore increases more rapidly with decreasing redshift. It is larger (smaller) than that in the HM2012 model at $z < 7$ ($z > 7$). The green squares in the lower middle panel show that we get a very similar clumping factor as HM2012 if we choose the same fixed self-shielding threshold of $\Delta_{\rm ss} = 100$. The small difference is due to a somewhat later reionization redshift in our small box ($z = 15$) compared to that of the simulations in Pawlik et al. (2009) ($z = 19.5$) on which the HM2012 prediction for the clumping factor is based. Once we choose the time evolution of Q_M to be same as in HM2012 in our default reionization model, the values of $\Gamma_{\rm HI}$ and $\lambda_{\rm mfp}$ are close to those in HM2012. At high redshift the photoionization rate is slightly higher as the photoionization rate within ionized regions is weighed inversely by the volume filling factor Q_V.

In our late reionization model the properties at $z \leq 6$ remain identical to the default model. At higher redshift, there are moderate changes in the quantities of interest as shown in Fig. 4. We find that in this model, the electron scattering optical depth is reduced to $\tau_{\rm el} = 0.072$ as opposed to $\tau_{\rm el} = 0.086$ in the default model. The value of $\tau_{\rm el}$ in the late reionization model is therefore lower than the 2013 Planck constraints obtained from Planck temperature and WMAP polarization data (Planck Collaboration et al. 2014), but is fully consistent with the latest Planck result $\tau_{\rm el} = 0.066 \pm 0.016$ (Planck Collaboration et al. 2015).

4 THE TRANSMISSIVITY OF THE Lyα LINE

4.1 Damping wings redwards of the systemic redshift

We now examine the Lyα opacity arising from the IGM in our models. To make contact with the earlier work of Bolton & Haehnelt (2013), we therefore first discuss the effects of the self-shielding prescription on Lyα absorption spectra. For this, we need to construct sightlines from the simulation box. We use the following method for calculating the absorption spectra: (i) we first extract sightlines parallel to the box boundaries through the most massive dark matter haloes in the simulation box. (ii) Each of these sightlines is spliced with other randomly drawn sightlines in the box to form a sightline of length $100\,h^{-1}$ cMpc. (iii) The Lyα optical depth, $\tau_{\rm Ly\alpha}$, is estimated along each line of sight given a value for $\Gamma_{\rm HI}$. We should mention that we do not attempt to model the complexities arising from radiative transfer within the host halo, hence as in Bolton & Haehnelt (2013) we ignore the contribution of any neutral gas within 20 pkpc of the centre of the host halo.

The distribution of the transmitted fraction, $\mathrm{e}^{-\tau_{\rm Ly\alpha}}$, for 600 such sightlines is shown in Figure 5 for two different values of the photoionization rates and for different self-

shielding prescriptions. The corresponding neutral volume fraction for these models are given in Table 1. In each panel, we show the median and 68 and 95 per cent bounds of the scatter around the median transmitted fraction. Without self-shielding (top panel), the median value of transmitted fraction recovers to nearly unity for rather small velocity shifts ($\sim$ 100 km s^{-1}) and the scatter is relatively small. As discussed in Bolton & Haehnelt (2013), in the SS model (middle panel) the transition is significantly reduced out to much larger velocity shifts due to the damping wing arising from optically thick regions. In addition, there is a large scatter around the median value once self-shielding is taken into account. For the SS-R model, the median value of the transmitted fraction is larger compared to the SS model, although not as large as in the No-SS case. However, *the scatter remains similar to that observed in the SS case.* This suggests that the spatial distribution of the transmitted fraction through the IGM will be highly variable when including the Lyα opacity in ionized regions – we will investigate this in the next section with maps of the spatial distribution of the Lyα emission line transmissivity. Note also we have *not* used any information from the large box, i.e., the large scale patchiness in the ionization field in this section.

4.2 The large scale distribution of the Lyα emission line transmissivity

Using the spatial neutral hydrogen distribution constructed as described in section 3, we are now in a position to investigate the large scale distribution of the transmissivity for the dark matter haloes expected to host Lyα emitters. An example of this is shown in Figure 6 for both our default and late reionization histories. We have identified the 250 most massive dark matter haloes in the small box and located the positions of all their copies in a $10\,h^{-1}$cMpc thick slab of the hybrid box. As the slab is populated with 100 shifted and rotated copies of the small box, this procedure yields 25000 sightlines towards these haloes for which we estimate the Lyα line transmissivity

$$T = \frac{\int_{\nu_{\rm min}}^{\nu_{\rm max}} {\rm d}\nu \; J(\nu) \; {\rm e}^{-\tau_{{\rm Ly}\alpha}(\nu)}}{\int_{\nu_{\rm min}}^{\nu_{\rm max}} {\rm d}\nu \; J(\nu)}, \qquad (8)$$

where $J(\nu)$ is the Lyα line profile. In this work, we take the shape of the profile to be Gaussian of width σ with its centre shifted redwards by an amount given by $\Delta v_{\rm int}$. We also account for the large-scale velocity fields from the large box (the details of this procedure and its effects are discussed in Appendix B).

The evolution of the transmissivity along these 25000 sightlines are shown as two-dimensional maps for a thin slice of our simulations in Figure 6 for our two reionization models. Note that the maps do not represent the expected distribution of transmissivity encountered by an observationally selected sample of Lyα emitters at that redshift, they show the value of T that a Lyα emitting galaxy would experience if it were located in the slice of the simulation for which the transmissivity is plotted. The maps are coloured according to the transmissivity of the nearest halo as seen in projection, where a 2D Voronoi tessellation is used for colouring the maps. The top two rows are for the default model, while the bottom two are for the late reionization model. For Figure 6 we have assumed the Lyα line to have a width $\sigma = 88$ km s^{-1} and to be shifted redward by an amount $\Delta v_{\rm int} = 100$ km s^{-1}, which at $z \sim 6$ is similar to values recently inferred from the CIII]λ1909 line (Stark et al. 2015). Note that this is a smaller velocity shift than the 200-400 km s^{-1} considered by Mesinger et al. (2015).

The mostly blue regions in Figure 6 are not yet reionized and transmission is very low. In the already ionized regions there is a large object-to-object scatter but as expected the median transmissivity is still substantially smaller than unity. The transmissivity thereby depends strongly on the intrinsic redshift and shape of the Lyα emission line. In Figure 7, we show the effect of various parameters on the transmissivity maps at a representative redshift of $z = 7$. The middle panel shows the default reionization model assuming the SS-R self-shielding model with $\sigma = 88$ km s^{-1} and $\Delta v_{\rm int} = 100$ km s^{-1}. The left and middle panels in the top row show how the modelling of the self-shielding affects the transmissivity. As before the SS-R prediction falls between those without self-shielding and the SS model. In the middle row we compare transmissivity maps for different values of the redward shift $\Delta v_{\rm int}$ of the emission line. With decreasing intrinsic redshift of the Lyα emission the transmissivity due to neutral hydrogen in the IGM in front of the emitters rapidly decreases. The bottom left panel shows the effect of reducing the line-width from $\sigma = 88$ km s^{-1} to $\sigma = 45$ km s^{-1} as a reduced intrinsic velocity shift may be correlated with a reduced line width due to the resonant nature of Lyman-alpha scattering. The average transmissivity increases somewhat for the reduced line width. For the somewhat larger line widths often observed at lower redshift (e.g., Shimasaku et al. 2006) the average transmissivity would be somewhat smaller than in our default model. The bottom middle panel shows the effect of peculiar velocities. As discussed in more detail in Appendix B, the effect of peculiar velocities is rather weak as the relevant gradients in peculiar velocity between host haloes and absorption from the surrounding IGM are rather small. Finally in the bottom right panel we show the case where the ionization field is constructed only from the large box, i.e., the ionized bubbles contain no neutral or partially ionized gas at all. As expected, in this case the transmission is only reduced behind not yet ionized regions.

The spatial patterns in transmissivity maps discussed above are due to a convolution of the underlying ionization field and the peculiar velocities of the Lyα host haloes and the intervening IGM. This spatial pattern will be further modified by spatial fluctuations in the photoionization rate within ionized regions, which our simulations do not yet model as we assume a single mean free path. Likely uncorrelated object-to object variation of the intrinsic spectral profiles of the Lyα emission and the spatial distribution of any Lyα absorbing dust will also modify this picture further. These transmissivity maps should nevertheless give a qualitative feel for the effect of the inclusion of the intervening Lyα opacity due to residual hydrogen in optically thick regions in otherwise already ionized regions. Note that the area of the GOODS-N and GOODS-S fields are smaller than the projected size of our large simulation box and that the transmissivity maps in Figures 6 and 7 suggest that there may be significant field to field variations for surveys of such angular area. More meaningful quantitative modelling of the

clustering of Lyα emitters (e.g. McQuinn et al. 2007; Jensen et al. 2013) which incorporates this will require more detailed modelling tailored to specific surveys, which we leave to future work.

4.3 The evolution of the observed Lyα equivalent width distribution and the rapid demise of Lyα emitters at $z > 6.5$

Having calculated the Lyα transmissivity due to neutral hydrogen for a large number of Lyα host haloes we are now in a position to reassess the effect of an inhomogeneously reionized intervening IGM on the evolution of Lyα emitters. Previous studies have done this by comparing to the observed $z = 6$ equivalent width distribution of Lyα emitters assuming it is not yet affected by the intervening IGM (e.g. Dijkstra et al. 2011) which is probably a good assumption for large velocity shifts $\Delta v_{\rm int} \sim 300 - 400$ km s^{-1}. However, as is apparent from Figure 6, the intervening IGM will affect the visibility also at $z \lesssim 6$ for lower values of $\Delta v_{\rm int} \sim 100$ km s^{-1}. Hence, for each model under consideration, we prefer to instead use the unabsorbed rest-frame Lyα equivalent width (REW) distribution $P_{\rm int}(>{\rm REW})$ that would be required to produce the observed $z = 6$ distribution $P_{z=6}(>{\rm REW})$ from Stark et al. (2011).[4] As in Mesinger et al. (2015) we consider the inferred REW distribution of observed UV-faint galaxies with $M_{\rm UV} > -20.25$ for which numbers are sufficient for a reasonably robust determination of REW upper limits.

Following Dijkstra et al. (2011), the REW distribution at any redshift z is calculated as

$$P_z(>{\rm REW}) = \int_0^1 {\rm d}T \; P_{T,z}(T) \; P_{\rm int}(>{\rm REW}/T), \qquad (9)$$

where $P_{T,z}(T)$ is the distribution of Lyα transmissivity T. Note that we have assumed that the unabsorbed distribution $P_{\rm int}(>{\rm REW})$ does not evolve with redshift and that there is no spatial correlation between the positions of potential Lyα emitters and ionized bubbles. As it is not known how strongly Lyα emitters are biased at $z > 6$ there is no obvious way of accounting for such a correlation. We will discuss later our third model where the positions of the Lyα emitters are assumed to be strongly correlated with the ionized regions. The resulting distributions are shown in Figure 8. In each panel, the dotted curves show the unabsorbed REW distribution that was chosen to reproduce the observed $z = 6$ REW distribution (Stark et al. 2011) for each model. The figure, thus, highlights the redshift evolution of the REW distribution. We also show data points at $z = 6$ (Stark et al. 2011), $z = 7$ (Ono et al. 2012; Pentericci et al. 2014) and the upper limit at $z = 8$ (Schenker et al. 2014; Tilvi et al. 2014). The top-left panel shows how the REW distribution evolves with redshift for the default and late reionization models with intrinsic velocity shift $\Delta v_{\rm int} = 100$ km s^{-1} and with our standard self-shielding prescription SS-R. The top-right panel shows the evolution when the ionized bubbles are assumed to contain no neutral hydrogen at all. Our default model is clearly unable to explain the rapid demise of the Lyα emitters between $z = 6$ and $z = 8$. The predicted REW distribution does not fall fast enough. Interestingly, our late reionization model matches the observed rapid fall at $z = 7$, and is close to (but still larger than) the upper limit at $z = 8$. The bottom-left panel of Figure 8 shows the effects of using a different (but also redshift-independent) redwards shift $\Delta v_{\rm int}$, while the bottom-right panel shows the effects of the self-shielding prescription at $z = 7$. Note that once the distribution is normalized to the observed points at $z = 6$ and the parameters and $Q_{\rm M}(z)$ are kept fixed, none of these choices make much of a difference to the predicted distribution at $z = 7$.

We confirm the findings of Keating et al. (2014) and Mesinger et al. (2015) that the effect of self-shielding of neutral hydrogen in LLSs is significantly reduced with the SS-R prescription compared to the SS prescription and is overall rather weak unless the photoionization rate is significantly lower than predicted by our models. As already discussed, however, we have probably underestimated the effect of self-shielding neutral gas for a variety of reasons: the missing large scale power in the matter distribution, the missing correlation of ionization and density fields on large scales and the neglect of fluctuations in the UV background amplitude and mean free path (e.g. Becker et al. (2015)).

In Figure 7 we had seen that the transmissivity depends rather strongly on the intrinsic velocity shift, $\Delta v_{\rm int}$, of the Lyα emission (see also Dijkstra et al. 2007; Laursen et al. 2011). The recent measurement of the velocity shift of Lyα emitters at $z \sim 6 - 7$ of about 100 km s^{-1} (Stark et al. 2015) is significantly smaller than the 300-400 km s^{-1} typically observed in LBGs at $z \sim 2$–3 (Steidel et al. 2010). It is not yet clear what causes this difference, but a plausible explanation is a decreasing neutral hydrogen column density (Barnes et al. 2011) as the interstellar medium in high-redshift galaxies becomes more ionized. This may also explain the postulated increase in the escape fraction of hydrogen ionizing photons with increasing redshift (Kuhlen & Faucher-Giguère 2012; Robertson et al. 2013; Ferrara & Loeb 2013; Becker & Bolton 2013). A rapidly decreasing $\Delta v_{\rm int}$ at $z > 6$ would contribute significantly to a decrease of the Lyα transmissivity and may be more plausible than the suggested rapid evolution of the Lyα equivalent width due to dust evolution (Dayal & Ferrara 2012). Note that smaller intrinsic velocity shifts also enhance the effect of the self-shielding on the transmissivity.

To explore this possibility, we have also investigated a model were the shift of the Lyα line, $\Delta v_{\rm int}$, is evolving with redshift,

$$\Delta v_{\rm int} = 100{\rm km\ s^{-1}} \left(\frac{1+z}{7}\right)^{-3}, \qquad (10)$$

which corresponds to a increase of about a factor two between $z = 8$ and $z = 6$ from 50 to 100 km s^{-1}. The results are shown in the left hand panel of Figure 9 where the solid lines are for the default model and the dashed lines are for the late reionization model. The default model combined with such an evolution of $\Delta v_{\rm int}$ still fails to match the rapid drop of the $z = 7$ data points. However, the late reionization model with a neutral fraction of ~ 30 (50) per cent at

[4] We find that a simple exponential function $P_{z=6}(>{\rm REW}) = \exp[-{\rm REW}/{\rm REW}_c]$ with ${\rm REW}_c = 41.5$Å fits the data points of Stark et al. (2011) quite nicely. The value of ${\rm REW}_c$ is somewhat smaller than used by Dijkstra et al. (2011) based on the data from Stark et al. (2010).

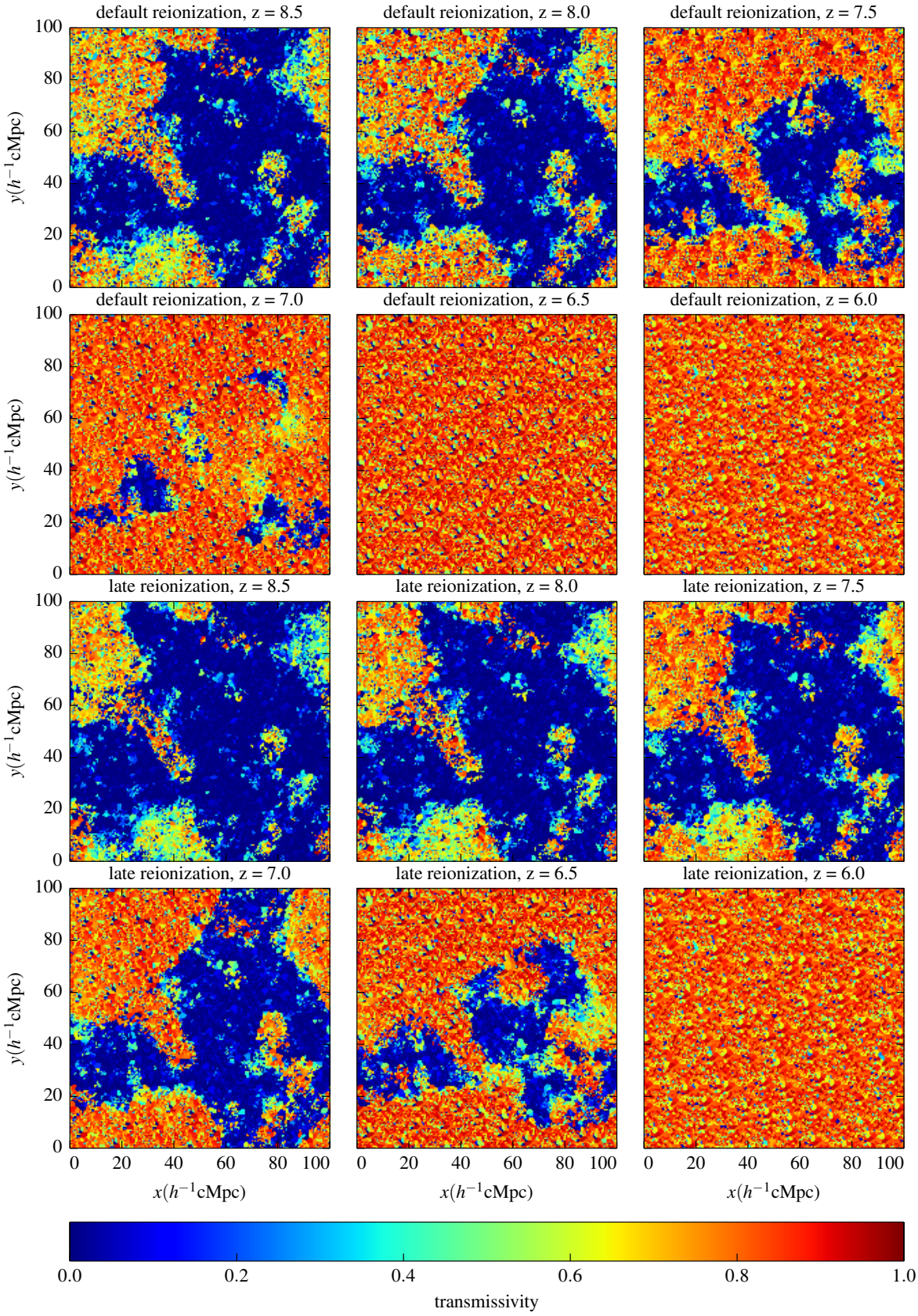

Figure 6. Maps of the transmissivity for Lyα emission lines at different redshifts. The two *upper* rows show results for the default reionization model, while the two *lower* rows show results for the late reionization model. The intrinsic velocity shift is $\Delta v_{\rm int} = 100$ km s^{-1}, and the width of the Lyα profile is $\sigma = 88$ km s^{-1}. The self-shielding is implemented according to the SS-R model. The maps are coloured according to the transmissivity of the nearest emitter as seen in projection.

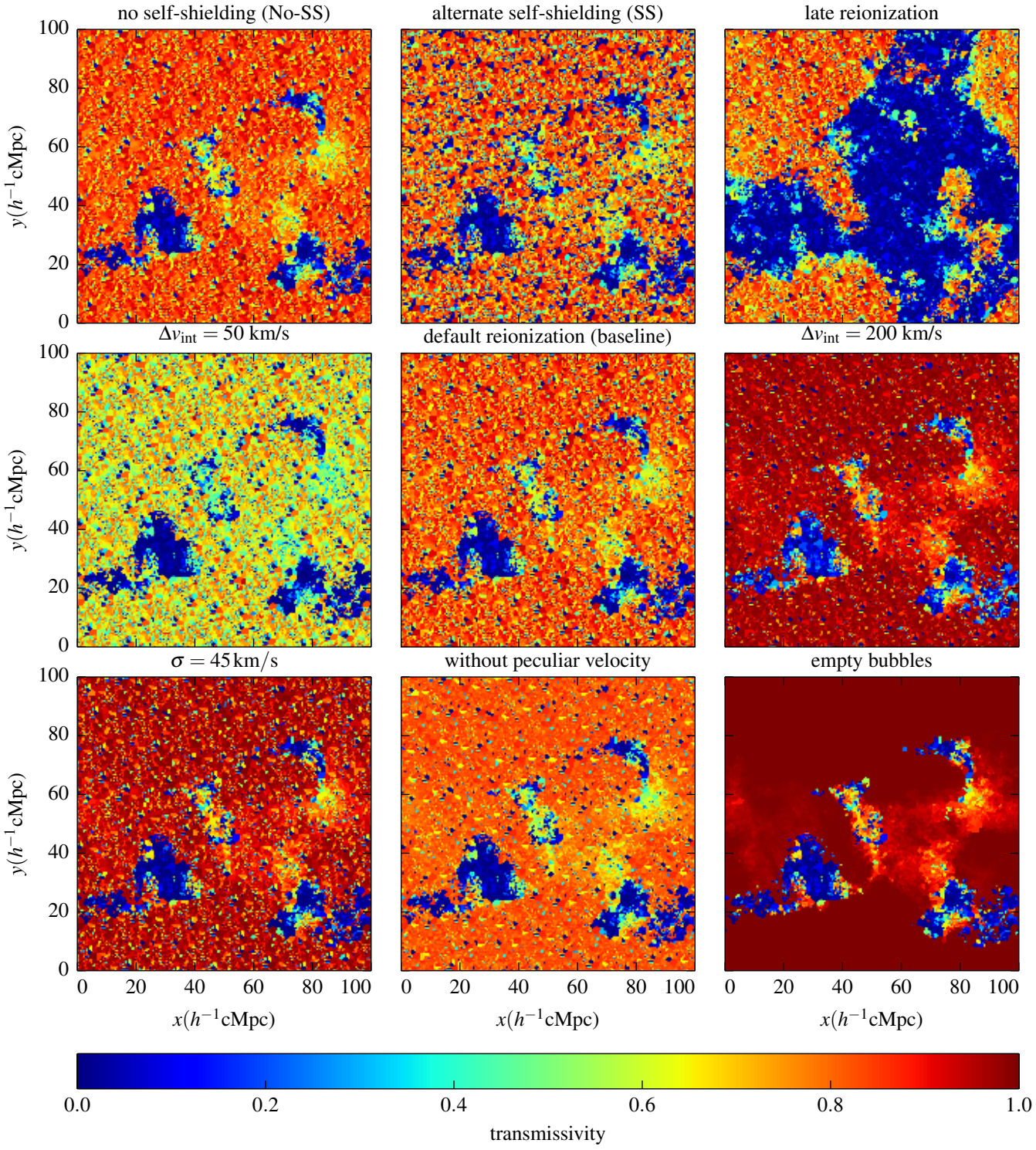

Figure 7. Maps of the transmissivity for Lyα emission lines for different model parameters. Results are shown at redshift $z = 7$. The baseline model shown in the *central* panel assumes the default reionization model, with $\Delta v_{\rm int} = 100$ km s^{-1}, $\sigma = 88$ km s^{-1}, the SS-R self-shielding model and peculiar velocities included (identical to the left panel in the second row of Fig. 6). The other panels show the effect of changing one of these assumptions at a time. Starting at the *top left* and going clockwise the panels show the transmissivity without self-shielding, with the SS self-shielding model, with the late reionization model, for $\Delta v_{\rm int} = 200$ km s^{-1}, ignoring absorbers in ionized bubbles, neglecting the effect of the peculiar velocity, for $\sigma = 45$ km s^{-1} and for $\Delta v_{\rm int} = 50$ km s^{-1}, respectively. The maps are coloured according to the transmissivity of the nearest emitter as seen in projection.

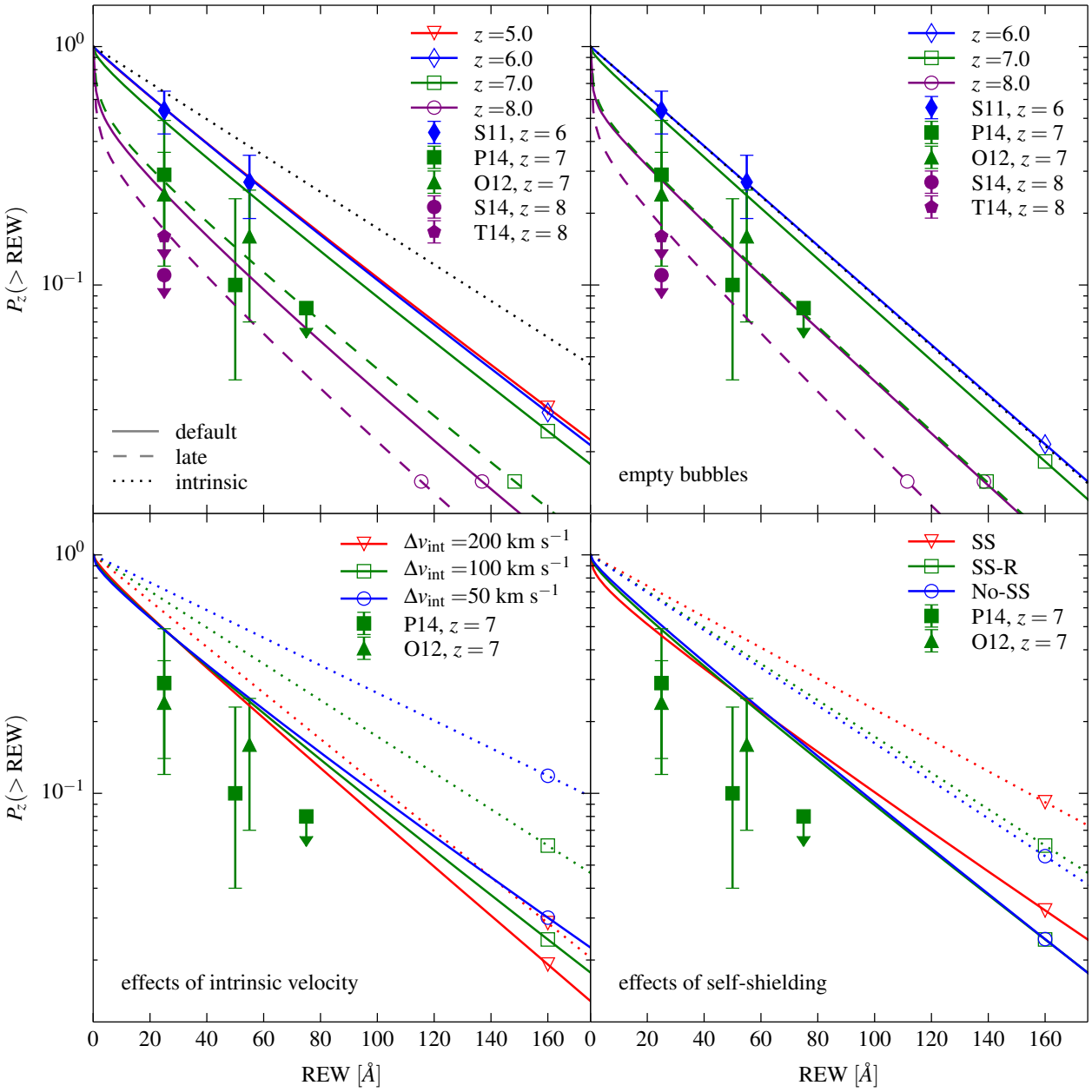

Figure 8. Cumulative probability distributions for the rest-frame Lyα equivalent width (REW). The dotted curves represent the intrinsic REW distribution that reproduces the observed $z = 6$ distribution for that parameter set. The points with error-bars represent the observed data for faint UV galaxies with $M_{\rm UV} > -20.25$ (Stark et al. 2011 - S11, composite data compiled by Ono et al. 2012 - O12, Pentericci et al. 2014 - P14, Schenker et al. 2014 - S14, Tilvi et al. 2014 - T14). The *top left* panel shows results for the default (solid curves) and late (dashed curves) reionization models assuming $\Delta v_{\rm int} = 100$ km s^{-1} , $\sigma = 88$ km s^{-1} and SS-R self-shielding. The *top right* panel shows results obtained ignoring all absorbers in ionized bubbles. All other parameters are unchanged. The *lower left* and *right* panels show the effects of changing $\Delta v_{\rm int}$ and the self-shielding prescription, respectively. Line markers have been added near the lower right corner of each panel to better facilitate identification of the different colours.

$z = 7$ ($z = 8$) is now consistent with the observed REW distribution.

In order to gauge the effect of possible correlations between the positions of the Lyα emitting galaxies and the ionized regions, we have also studied a rather extreme model where we place the Lyα emitters at the locations of the massive (i.e., $> 10^{10}$ M$_\odot$) haloes in the large box. Since sightlines towards haloes in the large box would not account for the expected larger (than average) number of self-shielded regions around the emitters, we choose the sightline toward the halo in the small box which is nearest to the massive halo in the large box. Further details of how we choose the haloes are given in Appendix C. To match the Lyα emitter data using this approach, we find a suitable $Q_M(z)$ by trial and error such that the reionization is completed at $z = 6$ (as opposed to 6.7 in HM2012) and evolves rapidly

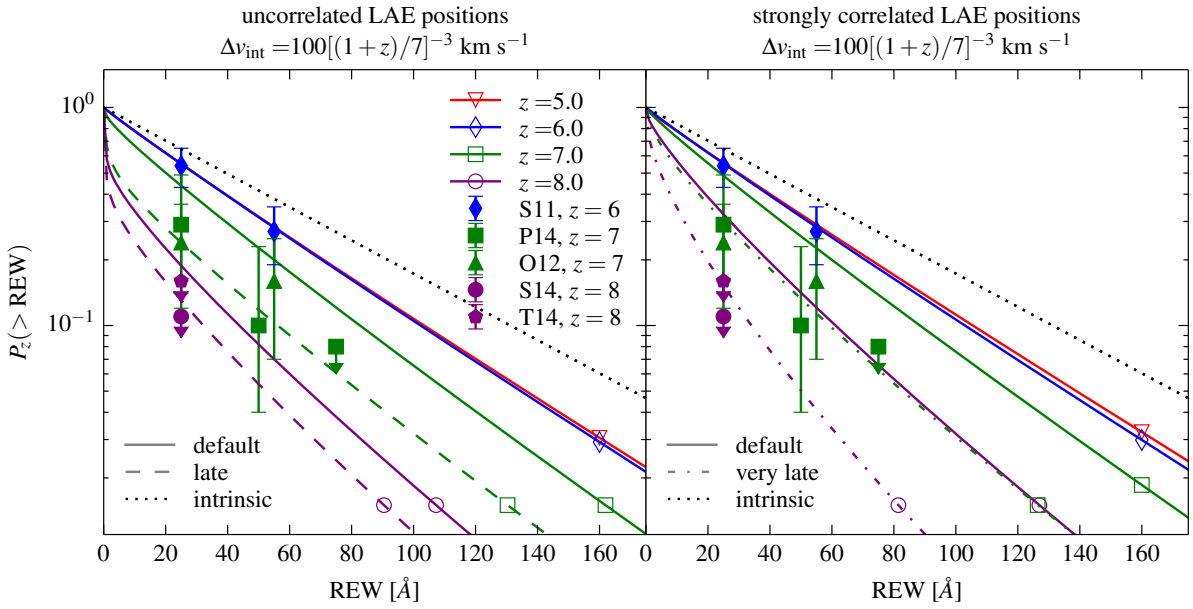

Figure 9. Evolution of the REW distribution when the intrinsic redward shift $\Delta v_{\rm int}$ of the Lyα line is assumed to evolve with redshift as $\Delta v_{\rm int} = 100{\rm km\ s^{-1}}\,[(1+z)/7]^{-3}$. The left hand panel is for the case where the correlation between Lyα emitters and ionized regions is ignored, while the right hand panel is for the case where the correlation is accounted for. All other parameter are the same as in the upper left panel of Fig. 8. The points with error bars represent the observed data for faint UV galaxies with $M_{\rm UV} > -20.25$ (Stark et al. 2011 - S11, composite data compiled by Ono et al. 2012 - O12, Pentericci et al. 2014 - P14, Schenker et al. 2014 - S14, Tilvi et al. 2014 - T14).

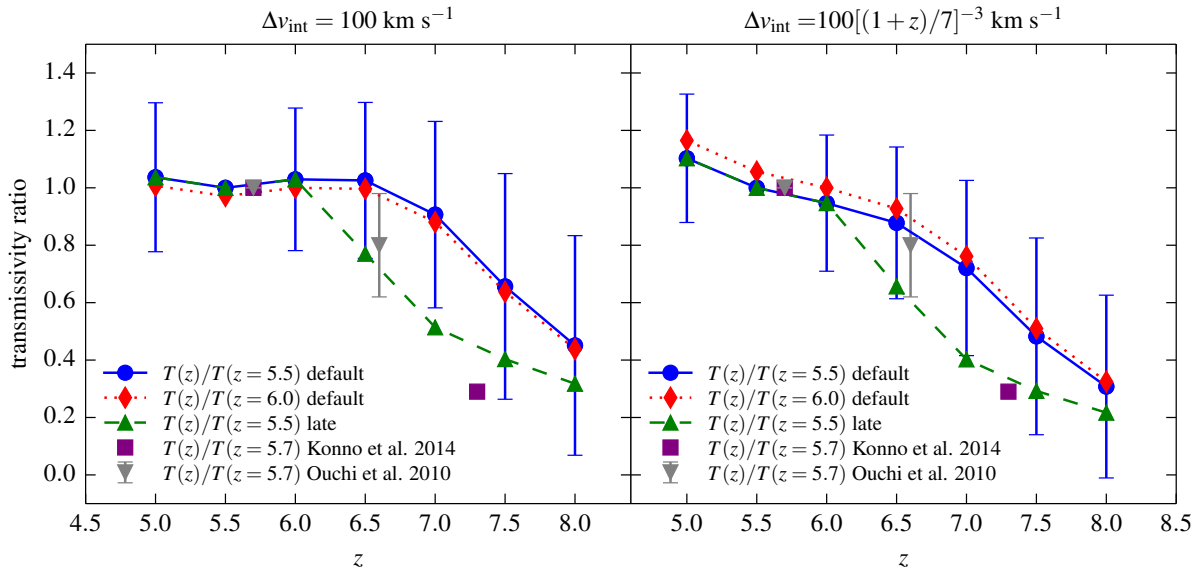

Figure 10. Evolution of the mean Lyα transmissivity of the IGM for the SS-R model, normalized to that at a particular redshift. The redward shift $\Delta v_{\rm int}$ of the Lyα line is 100km s^{-1} in the *left* panel and assumed to evolve with redshift as $\Delta v_{\rm int} = 100{\rm km\ s^{-1}}\,[(1+z)/7]^{-3}$ in the *right* panel. The observational constraints are from Ouchi et al. (2010) and Konno et al. (2014). The error bars on the simulation data display the 68 per cent scatter for the 25000 sight-lines considered.

at $z > 6$. Note that the evolution of $Q_M(z)$ in this model is considerably more rapid than in the late reionization model discussed earlier. The properties of this model, which we call the **very late reionization** model, are shown as light gray points and curves in Figure 4. The resulting REW distribution shown in the right hand panel of Figure 9 is again reasonably consistent with the data. Placing the Lyα emitters in haloes close to massive haloes in the large simulation box results in a very strong (probably unrealistically strong) correlation between the location of the ionized bubbles and that of the Lyα emitters for the simple collapse fraction model employed here for calculating the location of ionized bubbles. The smaller ionized mass fractions required for the

same reduction in transmissivity should thus probably better be considered as lower limits.

Finally, an alternative way to probe the Lyα transmissivity of the IGM is through the evolution of the Lyα luminosity function, corrected for changes arising from the evolution of the star formation rate density. Using the ultra-deep Subaru narrowband imaging survey for Lyα emitters at $z = 6.6$ in SXDS field, Ouchi et al. (2010) estimate the ratio of Lyα transmissivity at $z = 6.6$ and $z = 5.7$ to be $T(z = 6.6)/T(z = 5.7) = 0.80 \pm 0.18$. Similarly, using a survey at $z = 7.3$ in SXDS and COSMOS fields, Konno et al. (2014) estimate $T(z = 7.3)/T(z = 5.7) = 0.29$. In order to compare these results with our model predictions, we plot the evolution of the mean transmissivity as obtained from the maps shown in Figures 6 and 7 in Figure 10. The left panel assumes that $\Delta v_{\rm int} = 100$ km s^{-1}, while the right hand side is for the case when the intrinsic velocity shift evolves according to equation (10). The evolution of the transmissivity in our default model is again not rapid enough to account for observed evolution when $\Delta v_{\rm int}$ does not evolve, but the expected scatter is large. The error bars ($1\ \sigma$) show the object to object variation predicted by our model. As expected, the late reionization model is in better agreement with the data and matches rather well if $\Delta v_{\rm int}$ decreases at high redshift. The results for the very late reionization model, accounting for the correlation of the location of Lyα emitters and ionized regions, are again very similar to that of the late model.

5 CONCLUSIONS

We have combined high resolution hydrodynamical simulations with an intermediate resolution collisionless, dark matter only simulation and an analytical model for the growth of ionized regions to estimate the large scale distribution and redshift evolution of the visibility of Lyα emission in high-redshift galaxies. We have carefully calibrated the growth of ionized regions to that expected for the evolution of the UV-background model of HM2012, and included the Lyα opacity of intervening, optically thick absorption systems within ionized regions.

The rapid evolution of the ionized volume fraction, mean-free path and ionization rate of hydrogen at the tail end of reionization results in a rapidly evolving and strongly spatially variable transmissivity for the Lyα emission line. The Lyα transmissivity is thus very sensitive not only to the ionized volume fraction and amplitude of the local ionizing background, but also the relative velocity shift of the Lyα emission. Our default reionization model predicts an evolution of the Lyα REW distribution somewhat slower than observed, suggesting that additional factors contribute to the observed rapid demise of Lyα emission with increasing redshift at $z > 6$. The predicted evolution is also somewhat slower than that found in Bolton & Haehnelt (2013), mainly because of our improved modelling of the self-shielding of neutral hydrogen based on the results of the radiative transfer calculations by Rahmati et al. (2013).

We have furthermore identified the observed apparent decrease of the redwards shift of the intrinsic Lyα emission with increasing redshift (Stark et al. 2015) as an important factor which may contribute significantly to the evolution of the Lyα emission at $z > 6$. Interestingly such a decreasing redwards shift may be physically linked to the postulated increase in escape fraction of ionizing radiation (Kuhlen & Faucher-Giguère 2012; Robertson et al. 2013; Ferrara & Loeb 2013; Becker & Bolton 2013) and the expected lower neutral hydrogen column densities in high redshift galaxies at $z > 6$.

A model where reionization completes somewhat later and perhaps also more rapidly than assumed in the HM2012 UV background model, and where the intrinsic velocity shift of the Lyα emitters increases from 50 to 100 km s^{-1} between $z = 8$ and $z = 6$, matches the observed rapid decrease of the observed Lyα emission well. Based on the latest Planck results (Planck Collaboration et al. 2015), such a late reionization is no longer disfavoured by cosmic microwave background constraints. Accounting for the correlation of the location of ionized regions and Lyα emitters further strengthens this conclusion.

Forthcoming wide angle Lyα surveys aimed at at a better characterization of the large scale clustering properties of Lyα emitters at $z \sim 6-8$, together with further improved modelling of the spatial distribution of the Lyα emission line transmissivity of the kind we have presented here, should provide robust constraints on the timing and patchiness of the reionization of hydrogen.

ACKNOWLEDGEMENTS

Support by ERC Advanced Grant 320596 "The Emergence of Structure during the epoch of Reionization" is gratefully acknowledged. The simulations used in this work were performed on the Darwin and Cosmos supercomputers at the University of Cambridge. Part of the computing time was awarded through STFCs DiRAC initiative. JSB acknowledges the support of a Royal Society University Research Fellowship. We thank Richard Ellis, Brant Robertson and Mark Dijkstra for helpful comments.

REFERENCES

Barnes L. A., Haehnelt M. G., Tescari E., Viel M., 2011, MNRAS, 416, 1723
Becker G. D., Bolton J. S., 2013, MNRAS, 436, 1023
Becker G. D., Bolton J. S., Madau P., Pettini M., Ryan-Weber E. V., Venemans B. P., 2015, MNRAS, 447, 3402
Bolton J. S., Haehnelt M. G., 2013, MNRAS, 429, 1695
Bolton J. S., Haehnelt M. G., Warren S. J., Hewett P. C., Mortlock D. J., Venemans B. P., McMahon R. G., Simpson C., 2011, MNRAS, 416, L70
Bouwens R. J. et al., 2015, ApJ, 803, 34
Bouwens R. J. et al., 2013, ApJ, 765, L16
Calverley A. P., Becker G. D., Haehnelt M. G., Bolton J. S., 2011, MNRAS, 412, 2543
Caruana J., Bunker A. J., Wilkins S. M., Stanway E. R., Lacy M., Jarvis M. J., Lorenzoni S., Hickey S., 2012, MNRAS, 427, 3055
Caruana J., Bunker A. J., Wilkins S. M., Stanway E. R., Lorenzoni S., Jarvis M. J., Ebert H., 2014, MNRAS, 443, 2831

Choudhury T. R., Haehnelt M. G., Regan J., 2009, MNRAS, 394, 960
Dayal P., Ferrara A., 2012, MNRAS, 421, 2568
Dijkstra M., Lidz A., Wyithe J. S. B., 2007, MNRAS, 377, 1175
Dijkstra M., Mesinger A., Wyithe J. S. B., 2011, MNRAS, 414, 2139
Dijkstra M., Wyithe S., Haiman Z., Mesinger A., Pentericci L., 2014, MNRAS, 440, 3309
Emberson J. D., Thomas R. M., Alvarez M. A., 2013, ApJ, 763, 146
Faisst A. L., Capak P., Carollo C. M., Scarlata C., Scoville N., 2014, ApJ, 788, 87
Fan X. et al., 2006, AJ, 132, 117
Ferrara A., Loeb A., 2013, MNRAS, 431, 2826
Finkelstein S. L. et al., 2014, ArXiv e-prints
Fontana A. et al., 2010, ApJ, 725, L205
Gallerani S., Choudhury T. R., Ferrara A., 2006, MNRAS, 370, 1401
Gallerani S., Ferrara A., Fan X., Choudhury T. R., 2008, MNRAS, 386, 359
Haardt F., Madau P., 2012, ApJ, 746, 125
Hu E. M., Cowie L. L., Barger A. J., Capak P., Kakazu Y., Trouille L., 2010, ApJ, 725, 394
Iliev I. T., Mellema G., Shapiro P. R., Pen U.-L., Mao Y., Koda J., Ahn K., 2012, MNRAS, 423, 2222
Jensen H., Laursen P., Mellema G., Iliev I. T., Sommer-Larsen J., Shapiro P. R., 2013, MNRAS, 428, 1366
Kashikawa N. et al., 2006, ApJ, 648, 7
Kashikawa N. et al., 2011, ApJ, 734, 119
Keating L. C., Haehnelt M. G., Becker G. D., Bolton J. S., 2014, MNRAS, 438, 1820
Konno A. et al., 2014, ApJ, 797, 16
Kuhlen M., Faucher-Giguère C.-A., 2012, MNRAS, 423, 862
Labbé I. et al., 2013, ApJ, 777, L19
Laursen P., Sommer-Larsen J., Razoumov A. O., 2011, ApJ, 728, 52
Lukić Z., Stark C. W., Nugent P., White M., Meiksin A. A., Almgren A., 2015, MNRAS, 446, 3697
Madau P., Haardt F., Rees M. J., 1999, ApJ, 514, 648
Majumdar S., Bharadwaj S., Choudhury T. R., 2012, MNRAS, 426, 3178
Majumdar S., Mellema G., Datta K. K., Jensen H., Choudhury T. R., Bharadwaj S., Friedrich M. M., 2014, MNRAS, 443, 2843
McGreer I. D., Mesinger A., D'Odorico V., 2015, MNRAS, 447, 499
McLeod D. J., McLure R. J., Dunlop J. S., Robertson B. E., Ellis R. S., Targett T. T., 2014, ArXiv e-prints
McQuinn M., Hernquist L., Zaldarriaga M., Dutta S., 2007, MNRAS, 381, 75
Mellema G., Iliev I. T., Alvarez M. A., Shapiro P. R., 2006, New A, 11, 374
Mesinger A., Aykutalp A., Vanzella E., Pentericci L., Ferrara A., Dijkstra M., 2015, MNRAS, 446, 566
Mitra S., Choudhury T. R., Ferrara A., 2011, MNRAS, 413, 1569
Mitra S., Choudhury T. R., Ferrara A., 2012, MNRAS, 419, 1480
Mortlock D. J. et al., 2011, Nature, 474, 616
Oesch P. A. et al., 2013, ApJ, 773, 75
Oesch P. A. et al., 2014, ApJ, 786, 108
Ono Y. et al., 2012, ApJ, 744, 83
Ouchi M. et al., 2010, ApJ, 723, 869
Pawlik A. H., Schaye J., van Scherpenzeel E., 2009, MNRAS, 394, 1812
Pentericci L. et al., 2011, ApJ, 743, 132
Pentericci L. et al., 2014, ApJ, 793, 113
Planck Collaboration et al., 2014, A&A, 571, A16
Planck Collaboration et al., 2015, ArXiv e-prints, 1502, 1589
Pritchard J. R., Loeb A., Wyithe J. S. B., 2010, MNRAS, 408, 57
Rahmati A., Pawlik A. H., Raičevic M., Schaye J., 2013, MNRAS, 430, 2427
Raskutti S., Bolton J. S., Wyithe J. S. B., Becker G. D., 2012, MNRAS, 421, 1969
Robertson B. E. et al., 2013, ApJ, 768, 71
Schaye J., 2001, ApJ, 559, 507
Schaye J. et al., 2015, MNRAS, 446, 521
Schenker M. A., Ellis R. S., Konidaris N. P., Stark D. P., 2014, ApJ, 795, 20
Schenker M. A., Stark D. P., Ellis R. S., Robertson B. E., Dunlop J. S., McLure R. J., Kneib J.-P., Richard J., 2012, ApJ, 744, 179
Shimasaku K. et al., 2006, PASJ, 58, 313
Songaila A., Cowie L. L., 2010, ApJ, 721, 1448
Springel V., 2005, MNRAS, 364, 1105
Stark D. P., Ellis R. S., Chiu K., Ouchi M., Bunker A., 2010, MNRAS, 408, 1628
Stark D. P., Ellis R. S., Ouchi M., 2011, ApJ, 728, L2
Stark D. P. et al., 2015, MNRAS, 450, 1846
Steidel C. C., Erb D. K., Shapley A. E., Pettini M., Reddy N., Bogosavljević M., Rudie G. C., Rakic O., 2010, ApJ, 717, 289
Taylor J., Lidz A., 2014, MNRAS, 437, 2542
Tilvi V. et al., 2014, ApJ, 794, 5
Treu T., Trenti M., Stiavelli M., Auger M. W., Bradley L. D., 2012, ApJ, 747, 27
Vogelsberger M. et al., 2014, MNRAS, 444, 1518
Worseck G. et al., 2014, MNRAS, 445, 1745
Wyithe J. S. B., Bolton J. S., 2011, MNRAS, 412, 1926
Zahn O., Lidz A., McQuinn M., Dutta S., Hernquist L., Zaldarriaga M., Furlanetto S. R., 2007, ApJ, 654, 12

APPENDIX A: METHOD FOR GENERATING IONIZATION FIELDS

We outline here a more detailed description of the method we use to generate the ionization field for our hybrid simulations. The steps are as follows:

A1 Large scale ionization field

The first step is to generate the ionization field in the large box. We identify the haloes using a friends-of-friends group finder and assign emissivities proportional to the halo mass. These are subsequently used for generating the ionization field. A given location $\mathbf{x}$ in the simulation box is assumed to be ionized if, within a spherical region of radius R around

it, the condition

$$\zeta f_{\rm coll}(\mathbf{x}, R) \geq 1 + N_{\rm rec}(\mathbf{x}, R) \tag{A1}$$

is satisfied for any value of R. In the above expression, the quantity $f_{\rm coll}(\mathbf{x}, R)$ is the collapsed mass fraction and $N_{\rm rec}(\mathbf{x}, R)$ is the average number of recombinations within the spherical volume. The parameter ζ represents the number of photons in the IGM per hydrogen nucleus in stars and is given by

$$\zeta = f_* f_{\rm esc} N_\gamma, \tag{A2}$$

where f_* is the fraction of baryonic mass in stars, $f_{\rm esc}$ is the fraction of ionizing photons that escape into the IGM and N_γ is the number of ionizing photons produced per hydrogen atom in stars. In case the condition Eq. (A1) is not satisfied for any R, the location $\mathbf{x}$ is assigned a ionization fraction $\zeta f_{\rm coll}(\mathbf{x}, R_{\rm cell})/[1 + N_{\rm rec}(\mathbf{x}, R_{\rm cell})]$, where $R_{\rm cell}$ is the size of the grid cells.

The quantity $N_{\rm rec}(\mathbf{x}, R)$ will depend on the small scale clumpiness in the density field and on the reionization history in the spherical region around $\mathbf{x}$. We have already discussed that simulating the reionization history in a cosmologically representative volume along with resolving small scale features in the density field is a daunting task. In this work, we circumvent this difficulty by replacing $N_{\rm rec}(\mathbf{x}, R)$ with its globally averaged value $\bar{N}_{\rm rec}$. This approximation does not account for the fact that the number of recombinations will be larger when the spherical volume under consideration is centred around a high density region. However, the effect of this will be moderate towards the end stages of reionization where most of the ionized regions are so large that the average properties should be similar to the global averaged values.

With the above approximation and the definition

$$\zeta_{\rm eff} \equiv \frac{\zeta}{1 + \bar{N}_{\rm rec}}, \tag{A3}$$

the condition for a point to be ionized is simply given by equation (1). Note that we only need to specify the value of the one free parameter $\zeta_{\rm eff}$ at each redshift for generating the ionization field which is a combination of the properties of the halo (through the parameter ζ) and on the density structure (in particular, the clumping factor) and ionization history of the IGM (through $\bar{N}_{\rm rec}$).

A2 Ionization field in the hybrid box

As mentioned in Section 3, the ionization field in the hybrid box can be obtained by appropriately replicating the ionization field of the small box, and then superimposing the large scale neutral regions. Note that not all points in the IGM will have the background photoionization rate $\Gamma_{\rm HI}$. Firstly, when $Q_M < 1$, the large scale ionization field would not have percolated into certain regions, and hence we would have $\Gamma_{\rm HI} = 0$ in those neutral patches. In addition, the self-shielding condition will make the high density regions have a smaller photoionization rate even within ionized regions. Further, there will be spatial fluctuations in the background photoionization rate depending on the distribution of sources, especially before and immediately after the overlap of ionized regions. In this work we ignore such spatial fluctuations and assume the rate to be uniform within ionized regions. The only large scale fluctuations in $\Gamma_{\rm HI}$ thus arise from the distribution of ionized regions.

A3 Emissivity and other quantities of interest

Once the value of $\Gamma_{\rm HI}$ is known at every point in the hybrid box, it is straightforward to compute quantities like the emissivity $\dot{n}_{\rm ion}$, the mean free path $\lambda_{\rm mfp}$ of ionizing photons and the clumping factor $\mathcal{C}$.

The clumping factor $\mathcal{C} \equiv \overline{n_{\rm HII}^2}/\bar{n}_H^2$ is the most straightforward to obtain once the ionization field in the hybrid box is set up. The mean free path is obtained by shooting sightlines parallel to the box boundaries. We evaluate the optical depth $\tau_{\rm HI}(x) = \sigma_{\rm HI} \int^x {\rm d}x'\ n_{\rm HI}(x')$ at the Lyman-limit $\nu = \nu_{\rm HI}$ as a function of comoving distance x along each of these sightlines. The (comoving) mean free path is then given by

$$\lambda_{\rm mfp} = -\frac{x}{\ln \langle\, {\rm e}^{-\tau_{\rm HI}(x)} \,\rangle}, \tag{A4}$$

where $\langle \cdots \rangle$ denotes averaging over sightlines. One needs to choose the length x carefully, as too large a value would imply the optically thick limit $\left\langle\, {\rm e}^{-\tau_{\rm HI}(x)} \,\right\rangle \to 0$ thus the expression could lead to inaccurate values of $\lambda_{\rm mfp}$. It is thus optimal to choose x such that we can work in the optically thin limit $\left\langle\, {\rm e}^{-\tau_{\rm HI}(x)} \,\right\rangle \lesssim 1$, while still sampling a sufficiently large path length to take into account the self-shielding of optically thick systems. Following Emberson et al. (2013), we first calculate $\lambda_{\rm mfp}$ as a function of x and then choose the optimal ray length to be the largest value of x for which $x \leq \lambda_{\rm mfp}(x)/5$. Note that our calculation of $\lambda_{\rm mfp}$ accounts for the large scale ionization field in addition to the small scale high density systems.

The emissivity can be computed from $\Gamma_{\rm HI}$ and $\lambda_{\rm mfp}$ as given by Eq. (5). One can then feed in these values into Eq. (6) for Q_M and verify if the assumed value of ${\rm d}Q_M/{\rm d}t$ is recovered. If not, then one has to iteratively adjust the value of $\Gamma_{\rm HI}$ until convergence is achieved.

APPENDIX B: IMPLEMENTING LARGE SCALE VELOCITY FIELDS FOR THE TRANSMISSIVITY MAPS

We account for the differences in the peculiar velocities of emitting galaxies and absorbers by including information from both the small and the large box. The peculiar velocity field in the hybrid box is constructed by using the velocities at the appropriate position in the small box and adding the velocity corresponding to those Fourier modes in the large box that are not sampled in the small box, i.e. for which $|k_x| < \pi/(10\,{\rm Mpc}\,h^{-1})$, $|k_y| < \pi/(10\,{\rm Mpc}\,h^{-1})$ and $|k_z| < \pi/(10\,{\rm Mpc}\,h^{-1})$.

The effects of peculiar velocity on the Lyα transmissivity are illustrated in Fig. A1. In contrast to the intrinsic line redshift due to radiative transfer effects, the peculiar velocity of emitting galaxies and absorbers have little impact on the transmissivity; the relative velocity difference between host halo and absorber is typically small. The minor changes in the transmissivity are dominated by the small scale velocity field.

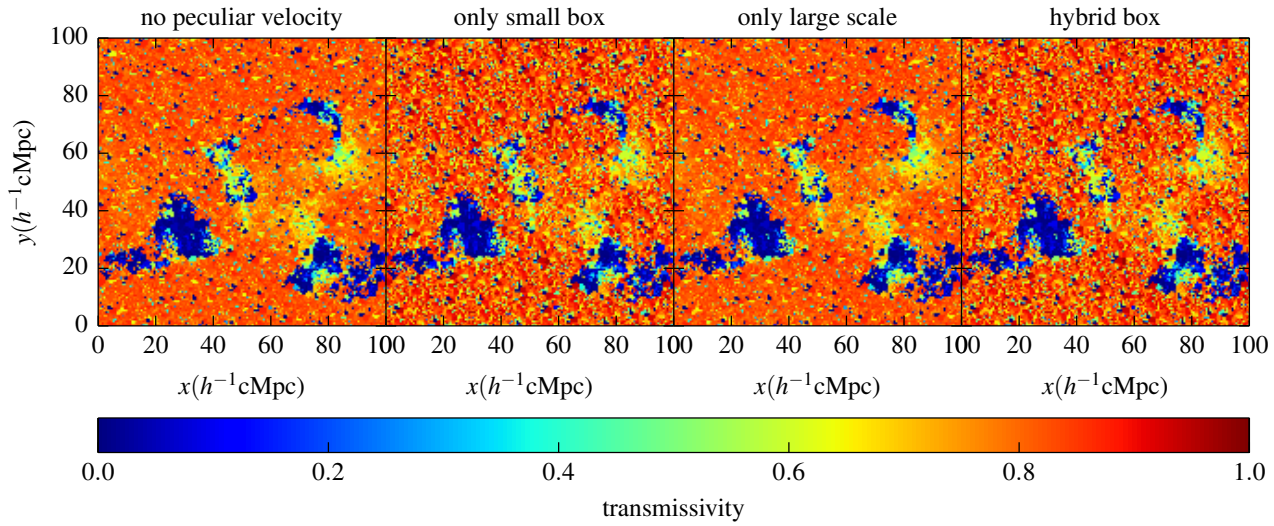

Figure A1. The effects of peculiar velocity on the Lyα emission line transmissivity. The *left panel* shows the transmissivity if peculiar velocities are ignored. In the *second* panel, we have accounted only for the peculiar velocities in the small box. The *third* panel displays results for which only the peculiar velocities in the large box have been used. Note, that here only those Fourier modes in the large box that are not sampled in the small box were included. The *right* panels shows the transmissivity in the hybrid box using the velocity field obtained by combining the velocities in the large and small boxes in Fourier space.

APPENDIX C: CORRELATIONS BETWEEN IONIZED REGIONS AND LYα EMITTING GALAXIES

As described in the main text in our default and late reionization models we have neglected possible spatial correlations between ionized regions and Lyα emitters while evaluating the effect of an increased neutral mass fraction on the visibility of observed Lyα emitters. How strongly correlated the ionized regions and Lyα emitters are is highly uncertain. To gauge the possible effect of such a correlation we have also considered an extreme model (the very late reionization model) where the Lyα emitters are placed close to the location of massive haloes in our large simulation box. For our simple collapse fraction model for identifying the ionized regions this results in a very strong correlation. In this model we assume that the Lyα emitters are hosted by haloes of mass $> 10^{10}$ $\mathrm{M}_{\odot}$ (Ouchi et al. 2010) in the large box. Since there is no correlation between the density fields in the large and small boxes in our hybrid simulation, sightlines towards haloes in the large box would, however, not account for the expected larger than average number of self-shielded regions in the vicinity of the Lyα emitters. Hence, for a given emitter identified in the large box, we take the sightline towards the halo in the small box which is nearest to the massive halo in the large box under consideration. We only consider the 250 most massive haloes in the small box for this. Note that this approach still does not account for the expected similar correlation of self-shielded and ionized regions, and hence will underestimate the effect of optically thick self-shielded regions on the Lyα emitter transmissivity. Reality should lie somewhere in between our uncorrelated and correlated models.

To match the observed evolution of Lyα emitters in this model, we have found a suitable $Q_M(z)$ by trial and error such that the reionization is completed at $z = 6$ (as opposed to 6.7 in HM2012) and evolves rapidly at $z > 6$. At high redshift some of the properties of the very late reionization model shown as light gray points and curves in Figure 4 exhibit significant differences compared to the default and late model without spatial correlations. The photoionization rate, in particular, shows a sharp rise at $z \sim 8$ due to the rather low values of Q_V. The ionizing photons produced are confined to smaller volumes and thus give rise to higher Γ_{HI}. At the same time the emissivity in this model is lower at high redshift to allow for a later start of reionization, followed by a sharp increase at $z \sim 6.5$. The electron scattering optical depth is reduced to $\tau_{\mathrm{el}} = 0.058$. The resulting REW distribution, as shown in the right hand panel of Figure 9, is again consistent with the data.

We thus see that irrespective of whether the correlation between Lyα emitters and ionized regions are modelled, it is possible to find reionization histories which are consistent with the CMB polarization data and at the same time able to explain the REW distribution of the observed Lyα emitters. Note, however, that the evolution of the ionized mass fraction is quite different in the different models, particularly towards the end of reionization.